

Supplementary Information

**Supercritical CO₂-constructed Intralayer [Bi₂O₂]²⁺ Structural Distortion for Enhanced CO₂
Electroreduction**

Authors:

Yannan Zhou,^{a‡} Pengfei Yan,^{a‡} Jun Jia,^a Suoying Zhang,^c Xiaoli Zheng,^a Li Zhang,^a Bin Zhang,^a Jun Chen,^d
Weichang Hao,^e Gongji Chen,^f Qun Xu,^{a,b,*} Buxing Han^{g,*}

Affiliations:

^aCollege of Materials Science and Engineering, Zhengzhou University, Zhengzhou 450052, P.R. China

Email: qunxu@zzu.edu.cn

^bHenan Institute of advanced technology, Zhengzhou University, Zhengzhou 450052, P.R. China

^cKey Laboratory of Flexible Electronics (KLOFE) & Institute of Advanced Materials (IAM), Nanjing Tech
University (Nanjing Tech), 30 South Puzhu Road, Nanjing 211816, P.R. China

^dInstitute of Innovative Materials, Innovation Campus, University of Wollongong, Northfields Avenue,
Wollongong, NSW 2500, Australia

^eCenter of Materials Physics and Chemistry, and Department of Physics, Beihang University, Beijing
100191, P. R. China

^fSupercomputing Center, Zhengzhou University, Zhengzhou 450052, P.R. China

^gBeijing National Laboratory for Molecular Sciences, Key Laboratory of Colloid and Interface and
Thermodynamics, Institute of Chemistry, Chinese Academy of Sciences, Beijing 100190, P.R. China

Email: hanbx@iccas.ac.cn (B.H.)

[‡]Y. Zhou and P. Yan contributed equally to this work.

Computational Methods

In order to explore the influence of Cl removal between $[\text{Bi}_2\text{O}_2]^{2+}$ layers on the structure of BiOCl (200) and the corresponding CO_2 adsorption configuration, the first-principles calculations based on density functional theory in the CASTEP plane-wave pseudopotential package with Perdew-Burke-Ernzerhof exchange-correlation function was performed.¹ For the pristine unit cells, the cutoff energy of the plane-wave basis was 550 eV, and $4 \times 4 \times 2$ k-points meshes were used for the Brillouin zone sampling.² Simultaneously, the electron-ion interactions were described by the ultrasoft pseudopotentials (USPPs),³ and the self-consistent field (SCF) calculation is kept within the energy convergence criterion of 1×10^{-6} eV atom⁻¹, and the Tkatchenko-Scheffler (TS) scheme was used for dispersion corrections.⁴ All the structures were optimized by using the Broyden-Fletcher-Goldfarb-Shanno (BFGS) minimization scheme. In addition, the surface of BiOCl (200) was simulated using a three-dimensional (3D) periodic slab model, the distance between two adjacent monolayers was larger than 15 Å to avoid the layer-layer interaction. The total energy was converged within 1×10^{-5} eV atom⁻¹, and the maximum force was converged within 0.03 eV Å⁻¹, while the maximum stress was converged within 0.05 GPa, the maximum atom displacement was converged within 0.001 Å. The lattice constants of the optimized BiOCl pristine unit cells are $a = b = 3.97$ Å, $c = 7.53$ Å.

Thermodynamic calculations and atomic model details

All thermodynamic calculations were performed using the ab initio software package (VASP).⁵ The DFT-D3 correction was considered to describe the Van der Waals interaction,⁶ and the cutoff energy of the plane wave basis set was chosen to be 540 eV. For the calculation of thermodynamic properties, $3 \times 2 \times 1$ k-points meshes were set for the multi-layer slab, and the grid spacing is $5 \times 4 \times 1$ for the few-layer slab. The energy and force convergence thresholds were set to 1×10^{-5} eV and 0.01 eV Å⁻¹. According to the structure of BiOCl nanoplates and BiOCl ultrathin nanosheets, two symmetrical models of BiOCl (200) lattice plane with various thickness were established to calculate Free energy, 2×2 supercell unit with 6 atomic layers and 2 atomic layers were used. The thickness of the vacuum layer was selected to 15 Å, and the bottom two layers were frozen at their equilibrium bulk positions, whereas the top four layers together with the adsorbates were allowed to relax (Fig. S22). It's noted that the thickness of the optimized values is 4.1 Å for BiOCl ultrathin nanosheets and 12.5 Å for distorted BiOCl nanoplates, respectively. Therefore, from the point view of geometric, the used thicknesses in calculation are in good agreement with the experimental data (3.75 Å, 12.75 Å), which also validates the rationality of our calculation models.

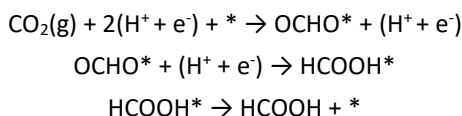
Free energy distribution was calculated to further establish their activity and selectivity by using the following Calculated Hydrogen Electrode Model (CHE).⁷

$$G = E_{\text{DFT}} + E_{\text{ZPE}} + \int C_v dT - TS$$

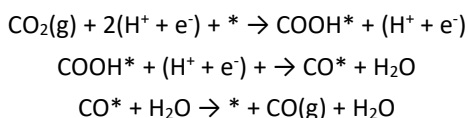
Among them, E_{DFT} is the calculated electron energy, E_{ZPE} is the zero-point vibration energy, $\int C_v dT$ is the enthalpy correction term, and TS is the entropy correction term.⁸

The possible reaction pathways of carbon dioxide reduction include the formation of formic acid, carbon monoxide, and competing reactions HER.

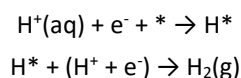
Formic Acid:



Carbon monoxide:



Hydrogen:



* denotes active site or adsorbed species on the empty surface.

Solvation effects on Gibbs free energy: The solvation free energy of adsorbates in equilibrium was calculated, and the free energy of the adsorbate and surface plate in vacuum state was subtracted. The stability of the adsorbates in the solvent was calculated via structural optimization.⁹

$$\Delta G_{\text{solvation}} = G_{\text{opt}} - (G_{\text{solvent}} + G_{\text{slab}})$$

Herein, we chose COOH*, CO*, and HCHO* intermediates adsorbed on a perfect surface as the representative models.^{10, 11} Previous work has reported that the effect of one-layer water on adsorbate was similar to that of multiple-layers water. Meanwhile, it is noted that the Grimme's DFT-D3 effect is not considered here in order to avoid any uncertainty. Our results show that the stable configuration of water layer on the perfect surface is hexagonal ice structure (Fig. S23), which is similar to the reported water layer structure on metal (111) surface.^{12, 13} Fig. S24 shows the structure of COOH*, CO*, and OCHO* intermediates adsorbed on the perfect surface. These intermediates are surrounded by one-layer water, and we can observe that their local structures are changed due to the interaction between adsorbates surface and solvent layer. The $\Delta G_{\text{solvation}}$ of adsorbed COOH*, OCHO*, and CO* intermediates in our work are 0.28, 0.21, and 0.11 eV in the presence of water molecules, respectively. It is noted that the solvation calibration of HCOOH* is not presented here, because physically adsorbed HCOOH* and HCOOH molecules are in the same environment.

Characterization

Powder X-ray diffraction patterns of all of the samples were collected at room temperature on a Bruker D8 Advance diffractometer using a germanium monochromatic (CuK α radiation, 40 kV and 40 mA). XRD data used for Rietveld refinement was carried out at a scan rate of 1° min⁻¹. The WAXS measurements were obtained at X-ray wide-angle scatterometer (France, Xenocs 2.0). X-ray photoelectron spectroscopy was performed using AXIS Supra system, all the binding energies were referenced to the C 1s peak at 284.6 eV of the surface adventitious carbon. SEM images were recorded using a Quanta 250 FEG FEI at 20 kV in gentle-beam mode without any metal coating. The X-ray absorption near edge structure (XANES) was obtained at the X-ray absorption fine structure station of Beijing Synchrotron Radiation Facility of the Institute of High Energy Physics, Chinese Academy of Sciences. The surface charge was analyzed by Zetasizer (Nano ZS90) apparatus in 0.5 M KHCO₃ aqueous solution. TEM images, Aberration-corrected HAADF-STEM images were observed by JEOL ARM-200F and a Tecnai G2 F20 operating at 200 kV.

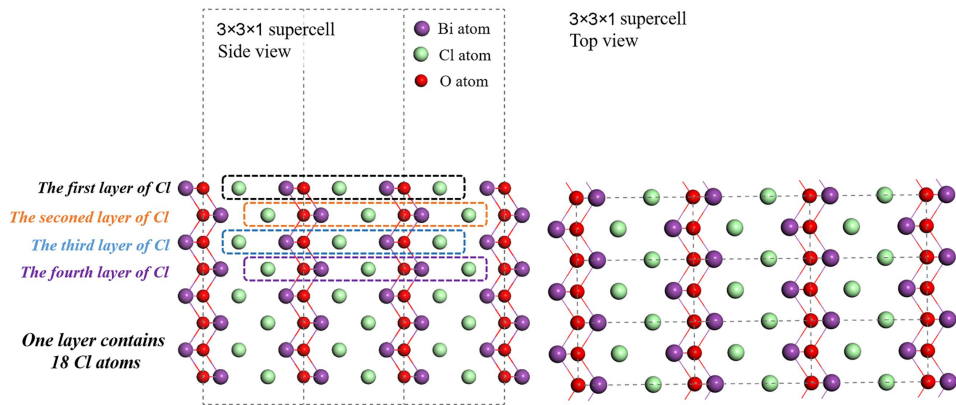


Fig. S1 The side view and top view of $3 \times 3 \times 1$ supercell of BiOCl (200) surface with a thickness of eight layers.

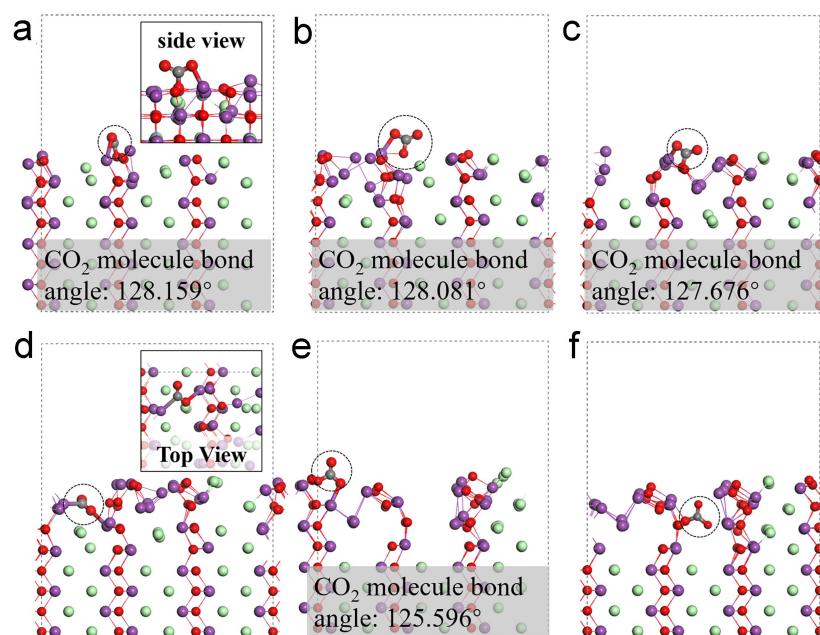


Fig. S2 Various adsorption configurations of CO₂ with an increasing number of Cl atoms removal. (a) one-layer Cl removed. (b) two-layers Cl removed. (c) three-layers Cl removed. (d) intralayer adsorption configuration with three-layers Cl removed. (e) four-layers Cl removed. (f) intralayer adsorption configuration with four-layers Cl removed.

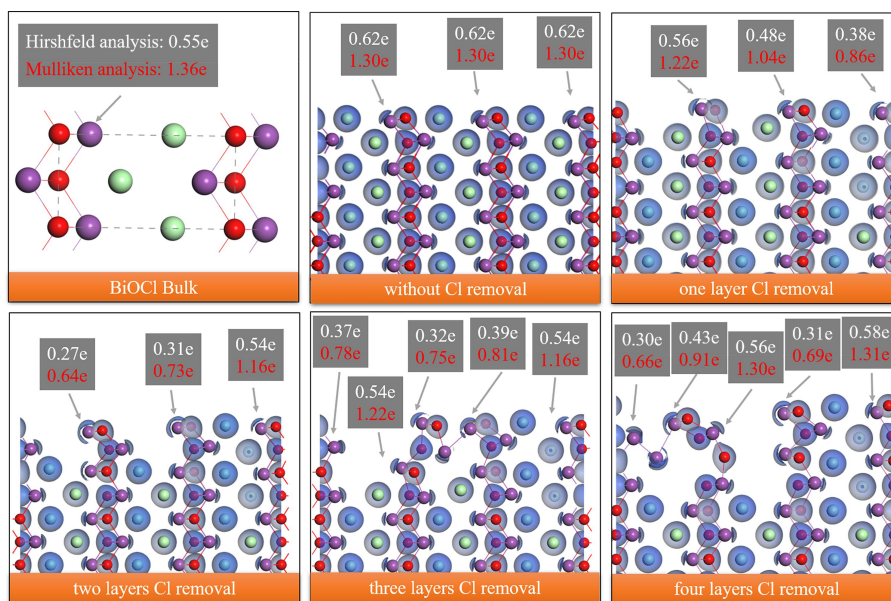


Fig. S3 The electron density diagram of BiOCl surfaces with varying removed Cl atoms, and the corresponding population analysis of Bi atoms. Red values are Mulliken analysis, white values are Hirshfeld analysis, and they both gradually change towards a more negative value with the decreased Cl atoms, indicating that resulted Bi atoms can capture more electrons. The value of isosurface is 0.35.

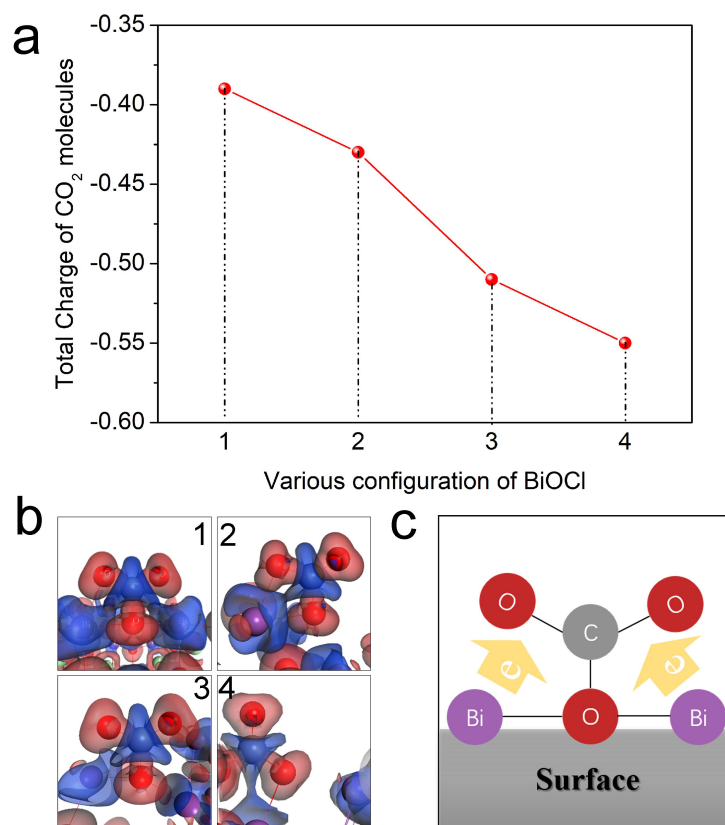


Fig. S4 Theoretical calculation. (a) The total charge of CO₂ adsorption on various configuration of BiOCl. Total charge refers to the algebraic sum of the Mulliken charges of C and O atoms in the adsorbed CO₂ molecule. The total charge value of free CO₂ molecule is zero, the more negative total charge value indicates more electrons captured by absorbed CO₂ molecule. (b) The different charge density diagram of configuration 1-4. Red means gaining electrons and blue means losing electrons, the value of isosurface is 0.4. (c) Proposed CO₂ adsorption configuration on distorted BiOCl surface. Bi atoms transfer electrons to adsorbed CO₂ molecules.

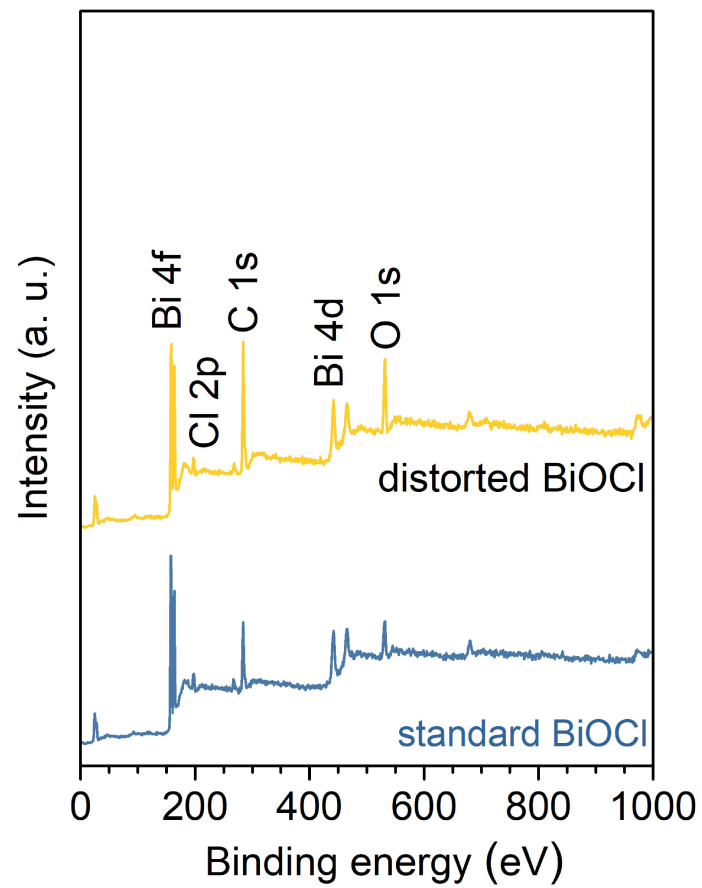


Fig. S5 XPS survey of standard BiOCl and distorted BiOCl nanoplates.

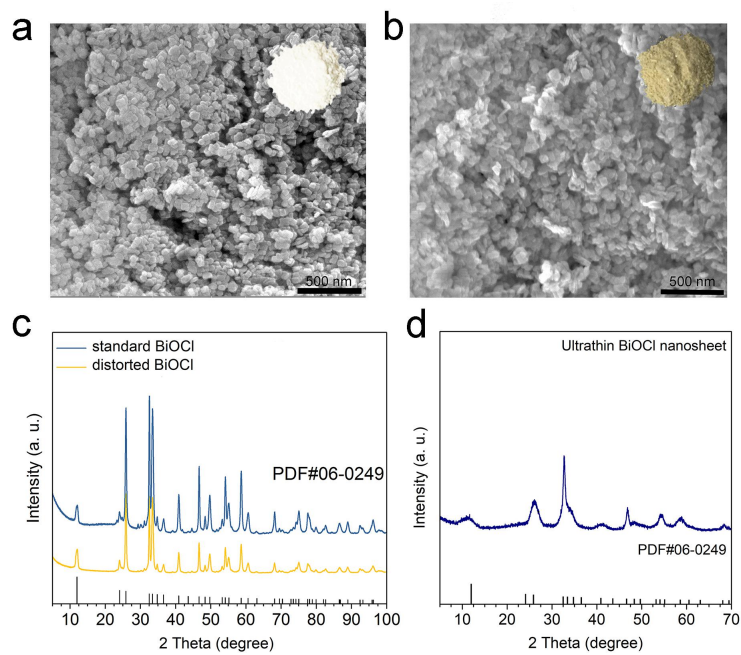


Fig. S6 Structural characterization. (a, b) SEM images of standard BiOCl and distorted BiOCl nanoplates. Inset: digital photograph. (c, d) Powder X-ray diffraction data of distorted BiOCl nanoplates and ultrathin nanosheets.

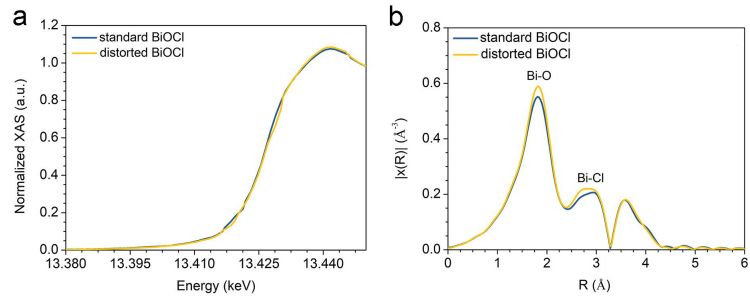


Fig. S7 Local electronic structure of standard BiOCl and distorted BiOCl nanoplates. (a) Bi L-edge XANES spectra. (b) Fitting results of the EXAFS spectra to R space.

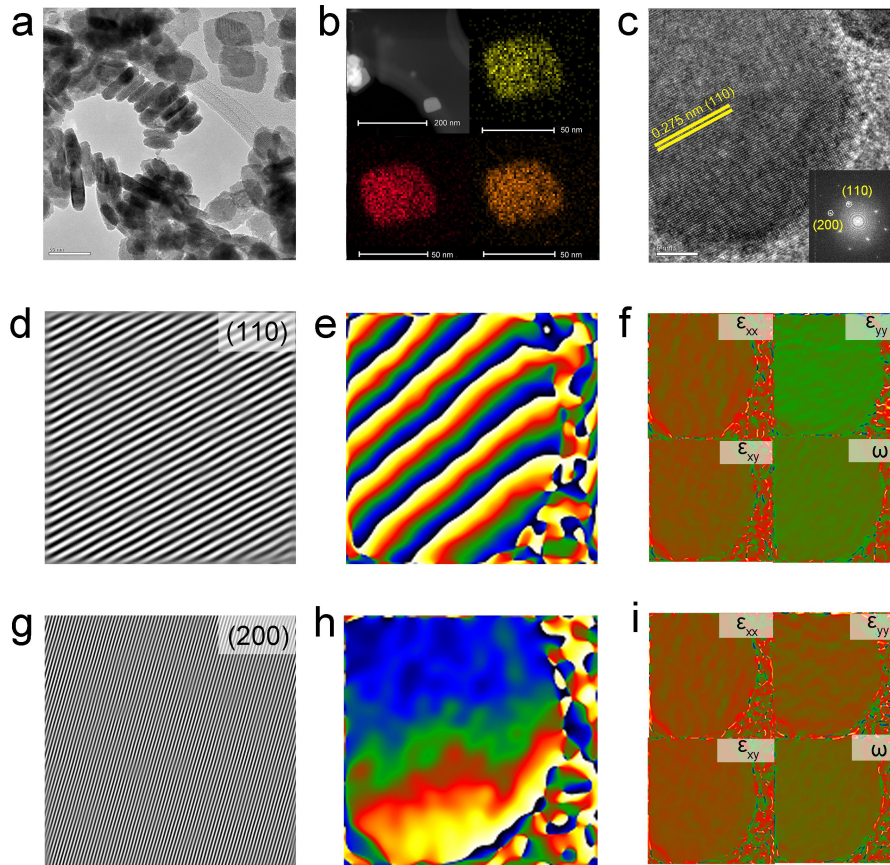


Fig. S8 Microscopic characterizations of standard BiOCl nanoplates. (a) TEM image. (b) STEM image and EDS mappings of Bi-L (yellow), O-K (red) and Cl-K (orange). (c) High-magnified TEM image and the resulted FFT. (d, g) Bragg filtered images of (110) and (200) reflection highlight the structural distortion. (e, h) GPA phase images of (110) and (200). (f, i) Strain maps of ϵ_{xx} , ϵ_{yy} , ϵ_{xy} and a rotation ω on different Bragg spots, the strain color scales with a range from -50% (black) to 50% (white).

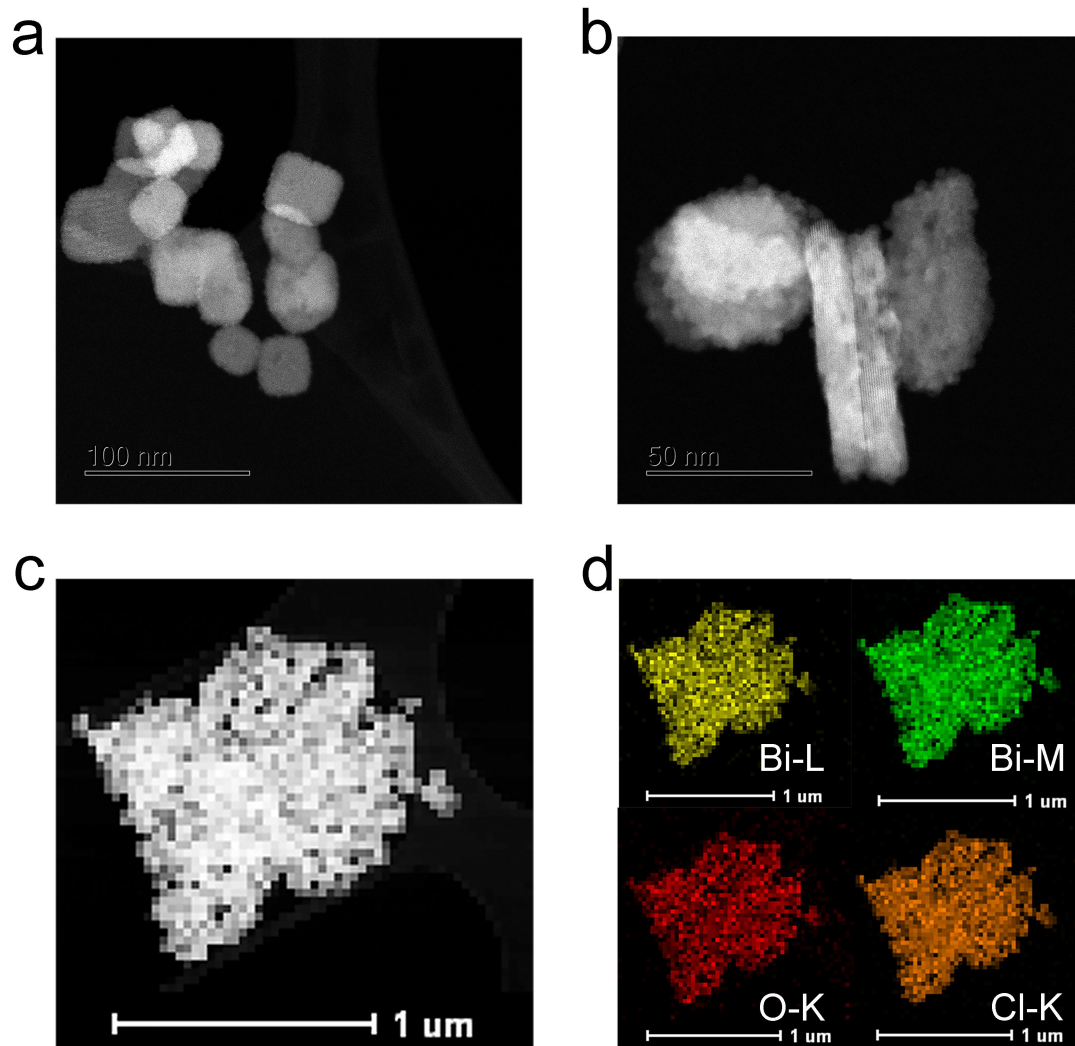


Fig. S9 Microscopic characterization of distorted BiOCl nanoplates. (a, b, c) STEM images. (d) EDS mappings of Bi-L (yellow), Bi-M (green), O-K (red) and Cl-K (orange).

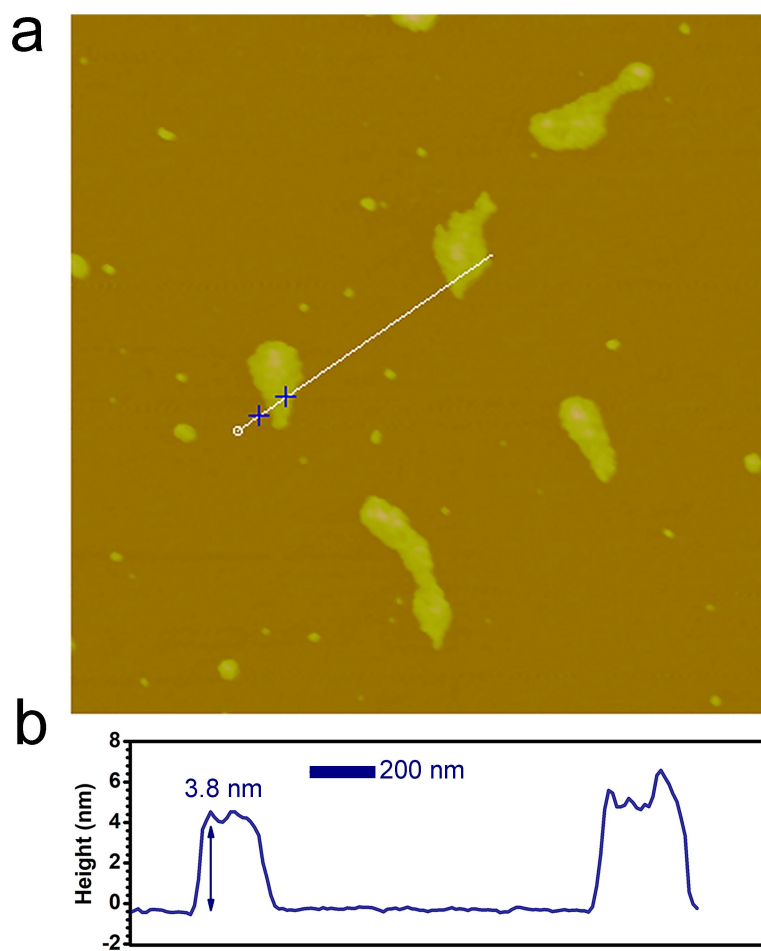


Fig. S10 Characterization of BiOCl ultrathin nanosheets. (a) Atomic force microscopic image. (b) the corresponding height profiles across nanosheets.

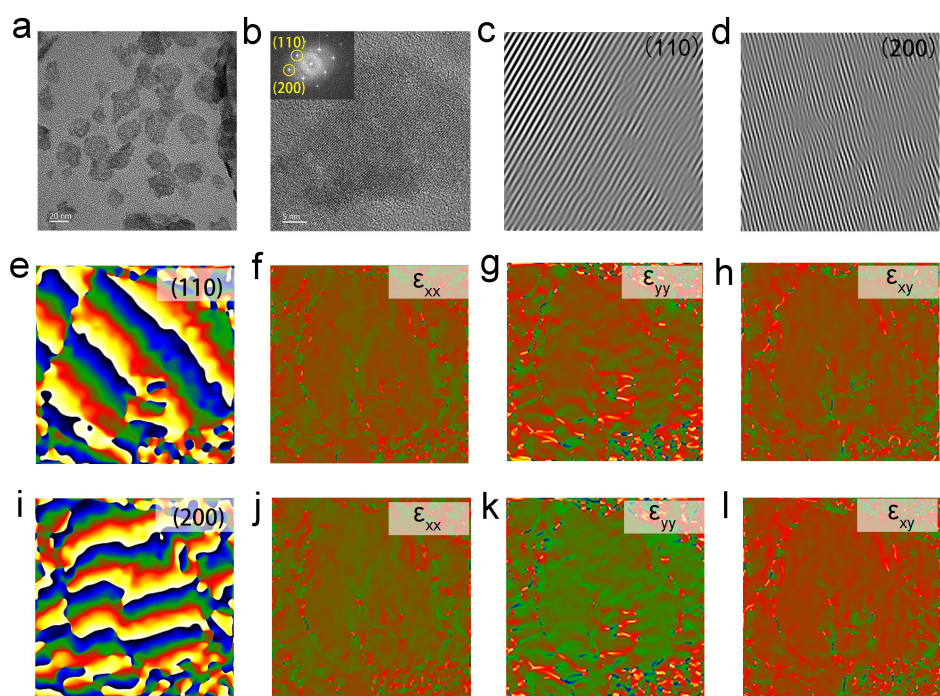


Fig. S11 Microscopic characterizations of BiOCl ultrathin nanosheets. (a) TEM image, (b) High-magnified TEM image, inset: FFT. (c, d) Bragg filtered images of (110) and (200) reflection highlight the structural distortion. (e, i) GPA phase images of (110) and (200). Strain maps of ϵ_{xx} (f, j), ϵ_{yy} (g, k), and ϵ_{xy} (h, l) on different Bragg spots, the strain color scales with a range from -50% (black) to 50% (white).

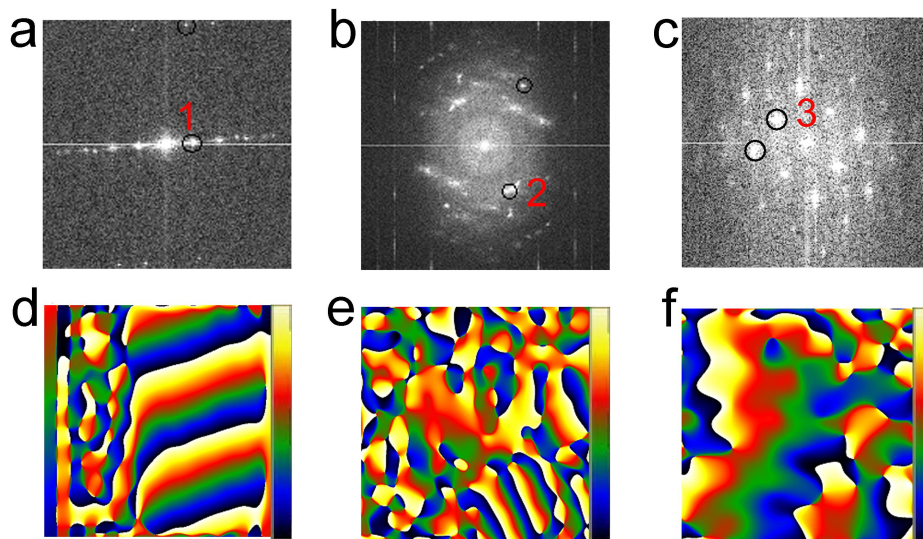


Fig. S12 (a, b, c) Fourier filtered images of HRTEM in Fig. 3. (d, e, f) GPA phase images from the corresponding Bragg spots in FFT.

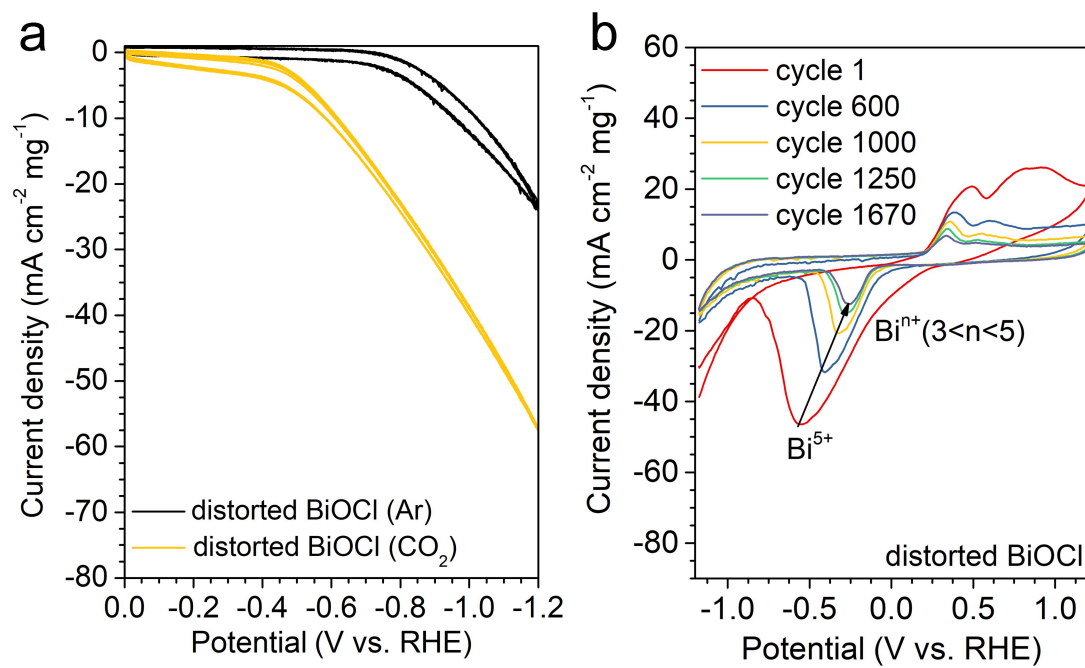


Fig. S13 CV curves of distorted BiOCl nanoplates at different potential window (100 mV s^{-1}). (a) between -1.2 V and 0 V , Ar- and CO_2 -saturated 0.5 M KHCO_3 . (b) between -1.2 V and 1.2 V , CO_2 -saturated 0.5 M KHCO_3 .

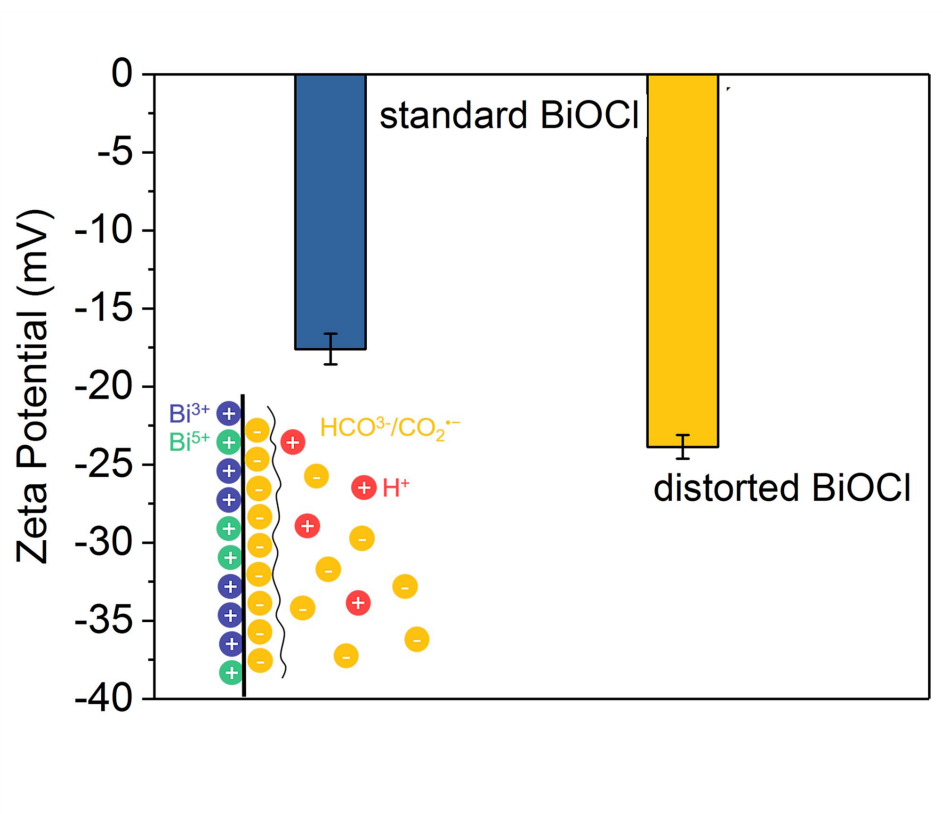


Fig. S14 Zeta potential measurement in 0.5 M KHCO_3 aqueous solution.

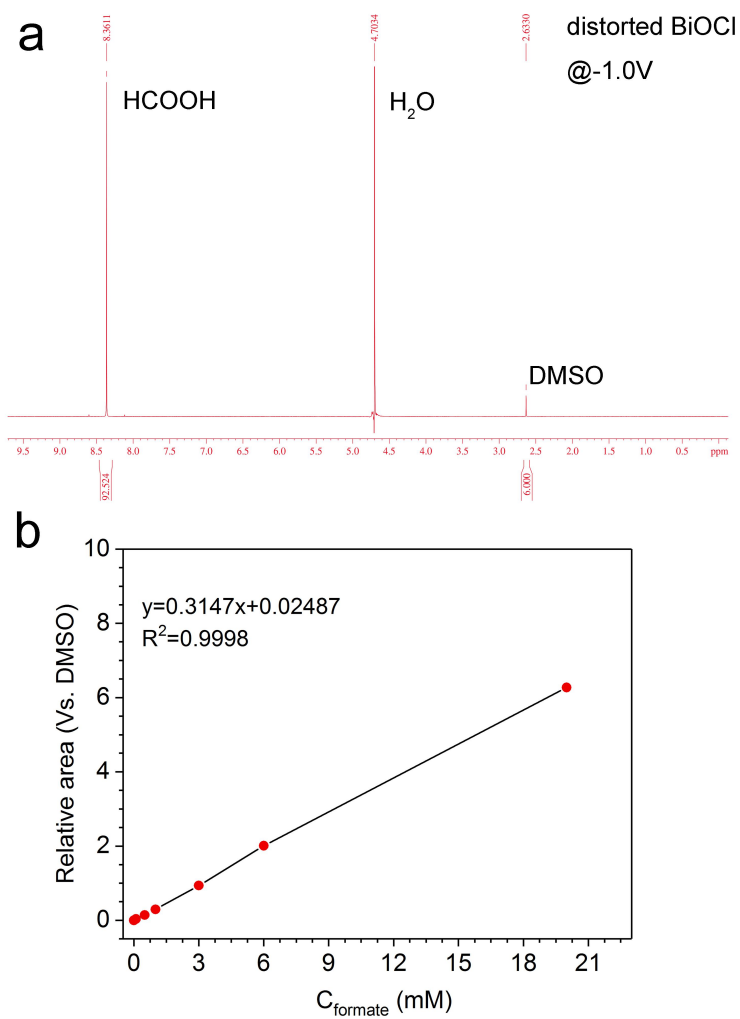


Fig. S15 Nuclear magnetic resonance data. (a) $^1\text{H-NMR}$ spectrum for qualitative determination of formate product at -1.0 V (vs. RHE) for 1.5 h. (b) Linear relationship between the given concentration of formate and relative area (vs. DMSO). The standard curve was measured from the reference samples prepared by mixing 0.49 mL of HCOOH (0.1, 0.5, 1, 3, 6, and 20 mM concentration) with 0.1 mL D_2O and 0.01 mL DMSO in 0.1 M KHCO_3 aqueous solution.

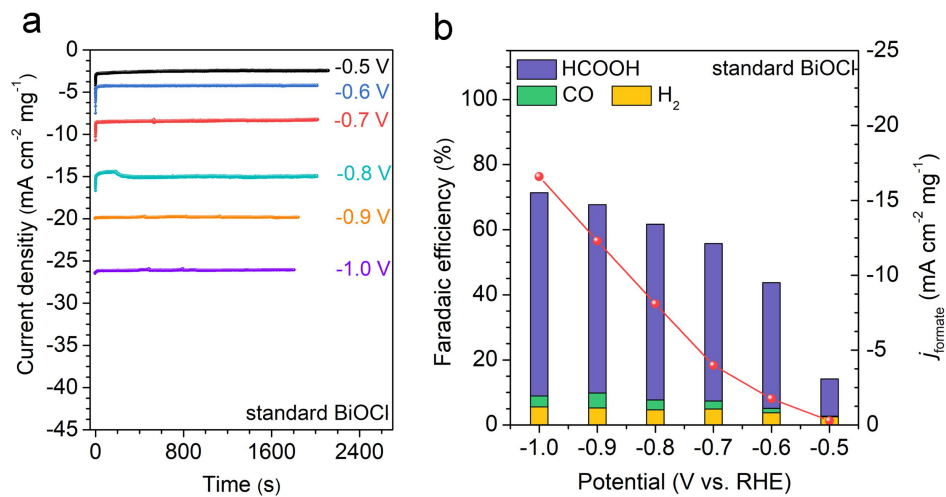


Fig. S16 Electrochemical CO₂ reduction on standard BiOCl nanoplates. (a) Chronoamperometry results in CO₂-saturated 0.5 M KHCO₃ at each given potential (vs. RHE). (b) Faradaic efficiencies of HCOO⁻, CO, and H₂ and HCOO⁻ partial current density at applied potential for 1700 s.

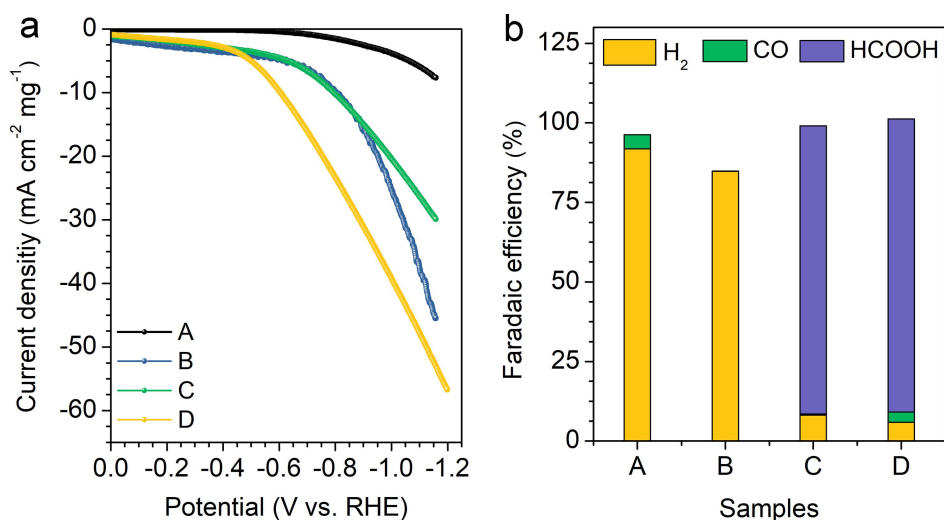


Fig. S17 (a) Linear sweep voltammetry curves in CO₂-saturated electrolytes. (b) Faradaic efficiencies of H₂, CO and HCOOH at -0.9 V vs. RHE for 1800 s. A: bare carbon paper, B: carbon powder, C: distorted BiOCl without carbon powder, D: distorted BiOCl and carbon powder.

To explore the role of carbon powder on the electrocatalytic performance, we have conducted the CO₂RR test for bare carbon paper, carbon powder and distorted BiOCl without carbon powder. As shown in Fig. S17, the introduction of conductive carbon powder indeed enhanced the CO₂RR activity with a higher current density compared with distorted BiOCl without carbon powder, especially at higher potential. In term of selectivity, both bare carbon paper and carbon powder show a high FE of nearly 80% toward H₂ evolution side reaction, while distorted BiOCl without carbon powder maintains high FE for HCOOH. Therefore, the current density of CO₂RR can be efficiently improved by adding carbon powder, whereas the high selectivity for HCOOH is dominated by distorted BiOCl.

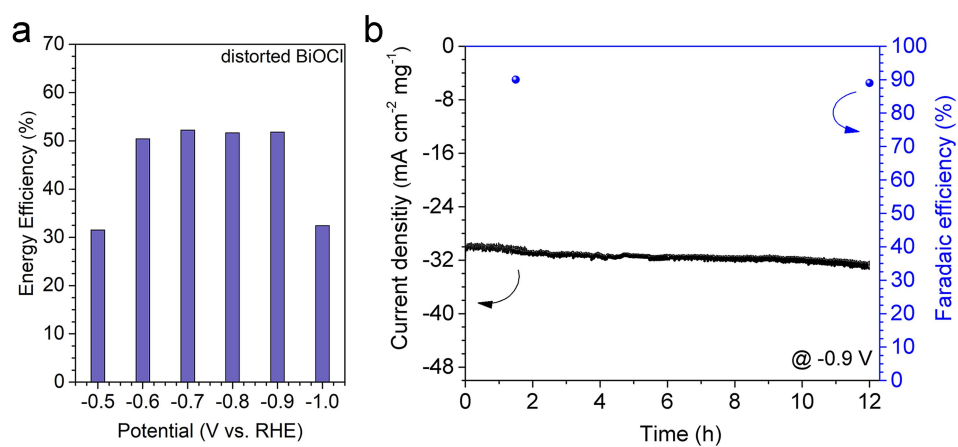


Fig. S18 CO₂RR evaluation of distorted BiOCl nanoplates. (a) Energy efficiency (EE) of distorted BiOCl. (b) Long-term stability tests of distorted BiOCl at -0.9 V (vs. RHE) for 12 h.

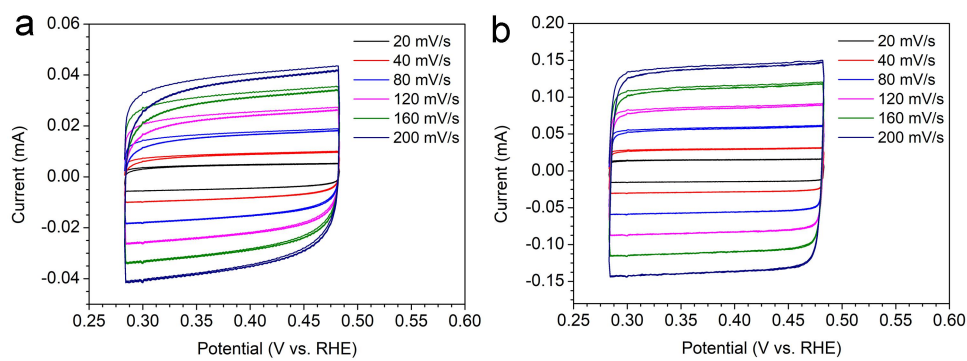


Fig. S19 Electrochemical surface area measurement. Cyclic voltammograms taken over a range of scan rates for standard BiOCl (a) and distorted BiOCl nanoplates (b), respectively.

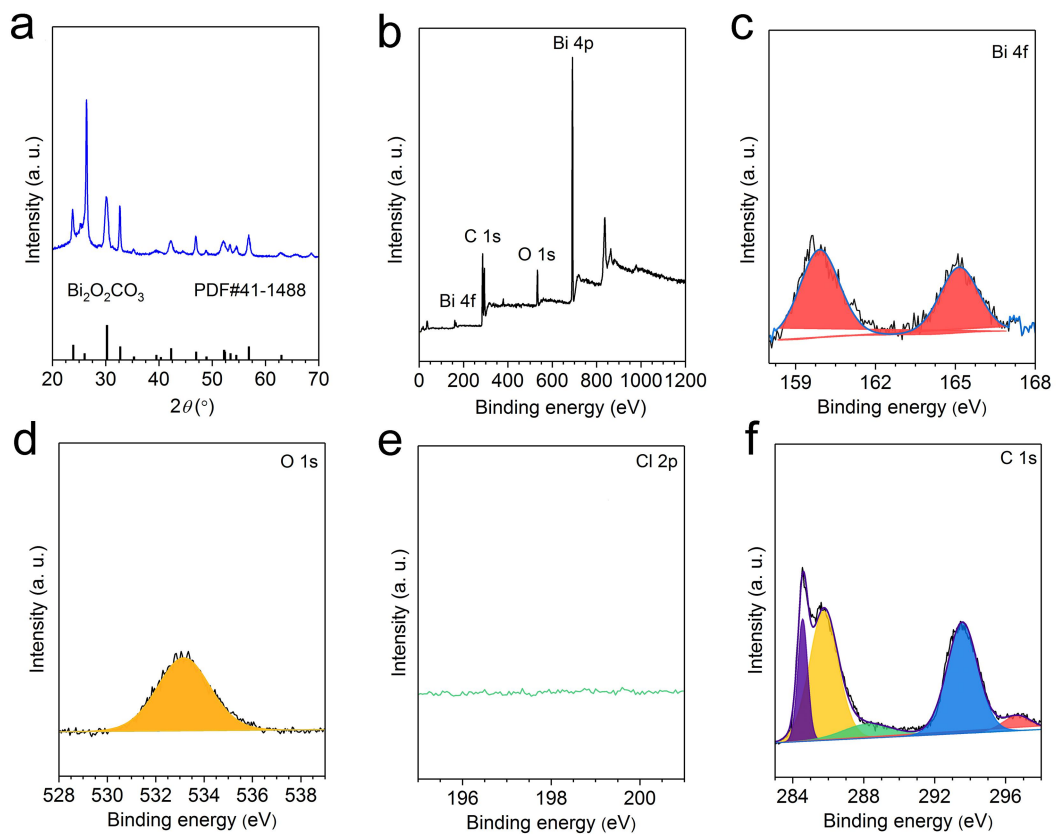


Fig. S20 Structure characterizations on the distorted BiOCl nanoplates after the long-term stability test. (a) XRD pattern. (b) XPS survey. (c) Bi 4f. (d) O 1s. (e) Cl 2p. (f) C 1s.

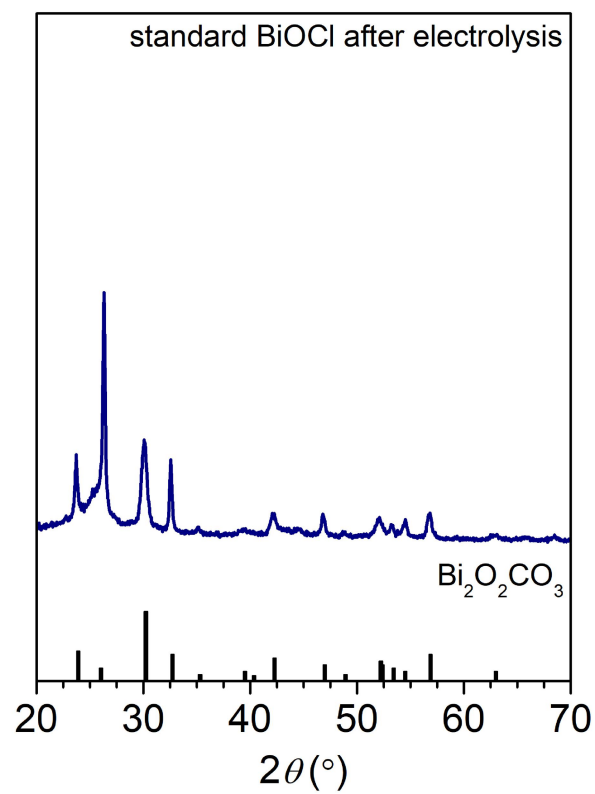


Fig. S21 XRD pattern of standard BiOCl nanoplates after CO₂RR test.

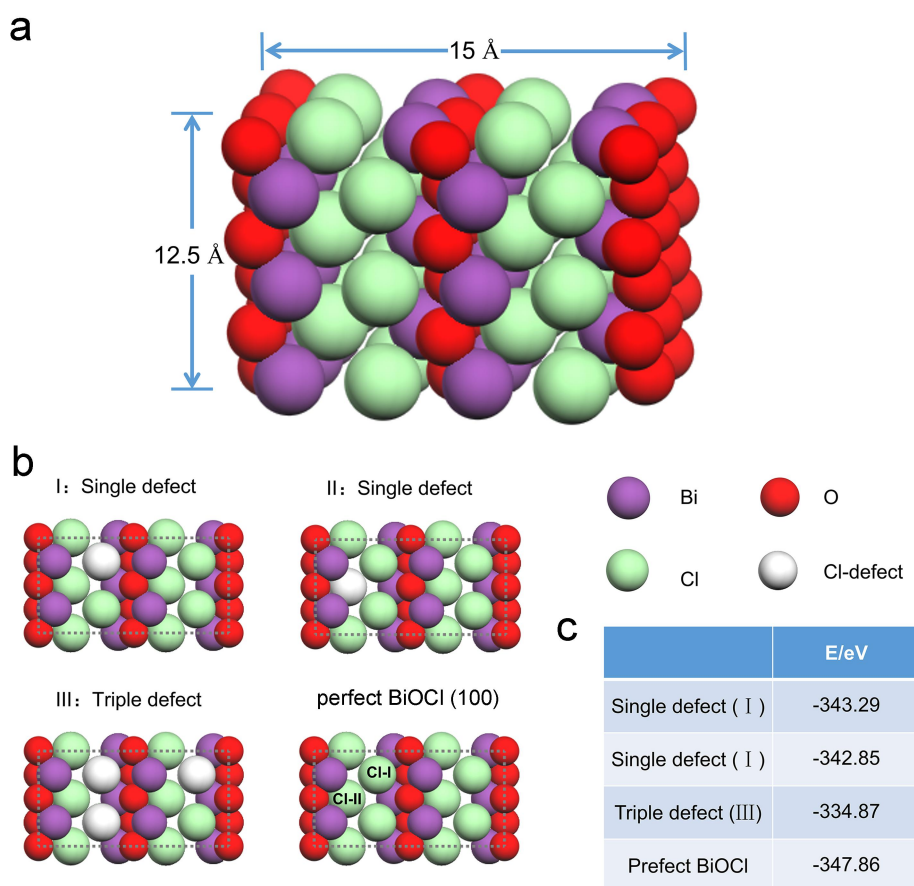


Fig. S22 (a) The surface unit cells of BiOCl (200), (b) the surface unit cell with various defect: (I, II) single defect, (III) triple defect, (c) total energy table for perfect BiOCl and defect-rich surface cell structure. Bi: purple, O: red, Cl: green.

Two different Cl atoms in perfect BiOCl are denoted as Cl (I) and Cl (II), Cl (I) connects with two Bi atoms, Cl (II) connects with one Bi atom. As shown in Fig. S22c, the total energy of single defect (I) surface structure is 0.44 eV lower than that of single defect (II), indicating that single defect (I) surface structure is more stable. Therefore, single defect (I) surface structure is the main defect configuration when single defect is created. Based on the total energy table, triple defect (III) is also a stable surface structure configuration.

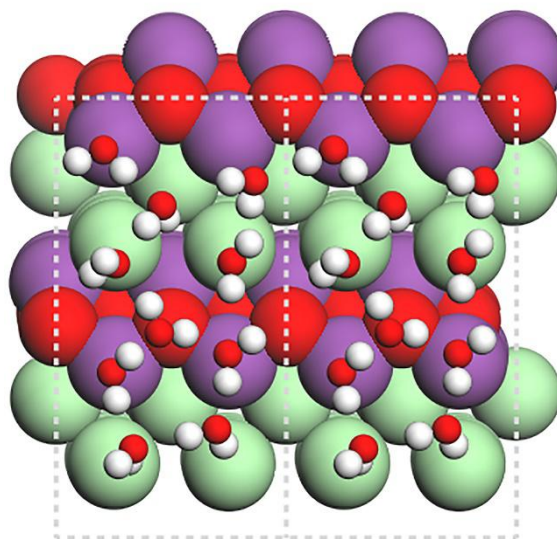


Fig. S23 Solvation model of H₂O molecules on the perfect surface (Top view).

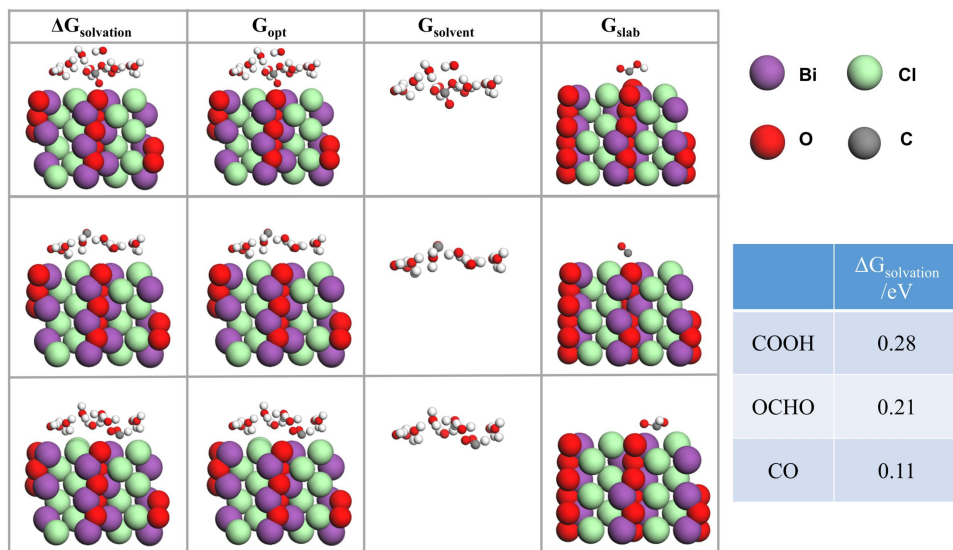


Fig. S24 The structure of COOH*, CO*, and HCHO* intermediates adsorbed on perfect surface in the presence of solvent layers. The good interaction between adsorbates surface and solvent layers can help to stabilize the whole system. G_{opt} refers to the optimal geometrical configuration of solvation model, and G_{solvent} refers to the water molecular layer. G_{slab} refers to a slab without water molecular layer. $G_{\text{solvation}}$ refers to the stable system achieved by the good interaction between adsorbates surface and solvent layer.

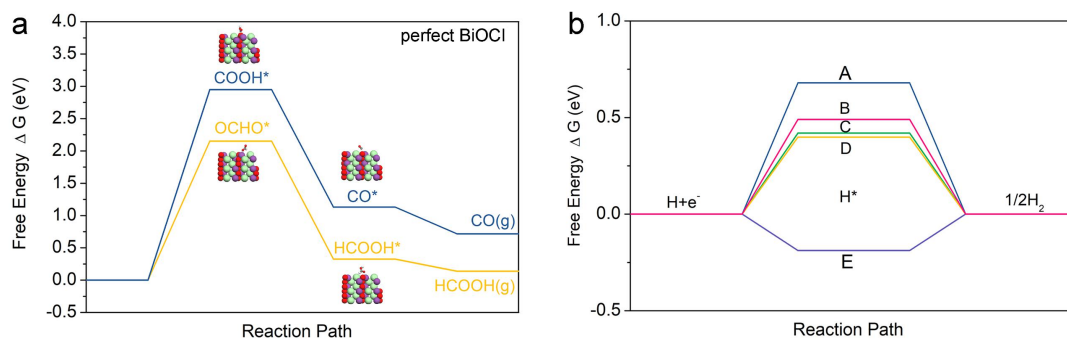


Fig. S25 (a) Free energy diagrams for CO and HCOOH on perfect BiOCl. (b) Free energy diagrams for H₂ on distorted BiOCl with triple Cl defect (A), distorted BiOCl with single Cl defect (B), standard BiOCl-V_O with oxygen defect (C), perfect BiOCl (D), and ultrathin nanosheets with single Cl defect (E).

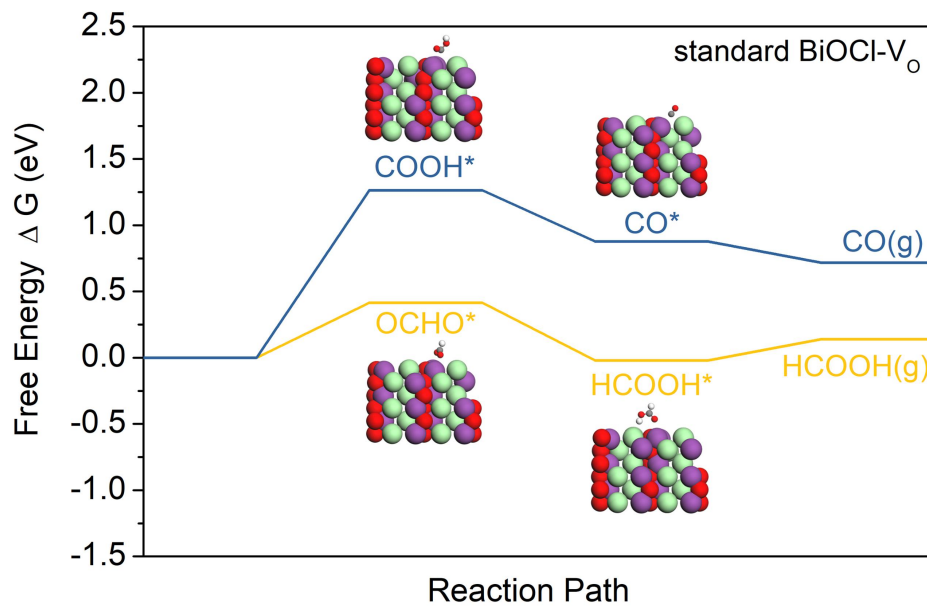


Fig. S26 Free energy diagrams for CO and HCOOH on standard BiOCl-V_O (Side view).

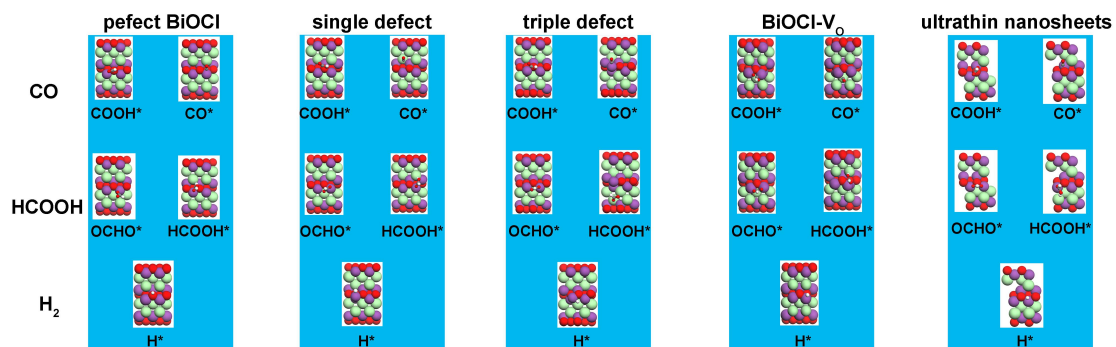


Fig. S27 Optimized geometric structure of various adsorbed intermediates for CO, HCOOH and H₂ path way on (200) planes of perfect BiOCl, distorted BiOCl with single Cl defect, distorted BiOCl with triple Cl defect, standard BiOCl-V_o with oxygen defect, ultrathin nanosheets with single Cl defect. Top view.

Table S1. Hirshfeld charge analysis and orbital population analysis of active sites (Bi and O atoms) with various Cl atom layers removal, and the resulted corresponding CO₂ adsorption energy.

Depth of Cl removal	Hirshfeld Analysis		Orbital Populations		CO ₂ molecules Adsorption energy
0	Bi	0.62e	S	1.941	None
			Px	0.574	
			Py	0.593	
			Pz	0.568	
	O	-0.38e	S	1.932	
			Px	1.538	
			Py	1.647	
			Pz	1.742	
1	Bi	0.38e	S	1.936	-0.19eV
			Px	0.512	
			Py	1.152	
			Pz	0.523	
	O	-0.38e	S	1.95	
			Px	1.508	
			Py	1.703	
			Pz	1.689	
2	Bi	0.27e	S	1.941	-3.13eV
			Px	0.496	
			Py	0.688	
			Pz	1.234	
	O	-0.37	S	1.935	
			Px	1.535	
			Py	1.587	
			Pz	1.794	
3	Bi	0.32e	S	1.934	-3.54eV
			Px	0.562	
			Py	1.141	
			Pz	0.611	
	O	-0.34e	S	1.962	
			Px	1.527	
			Py	1.694	
			Pz	1.623	

Table S2. Fitting parameters of the EXAFS spectra of standard BiOCl and distorted BiOCl nanoplates. R: distance; σ^2 : mean-square disorder.

Samples	Scattering path	CN	σ^2	R(\AA)	R-factor
standard BiOCl	Bi-O	4	0.0097(0.0008)	2.290(0.008)	0.003
	Bi-Cl	4	0.0231(0.0021)	3.053(0.008)	
	Bi-Bi1	4	0.0067(0.0005)	3.714(0.008)	
	Bi-Bi2	4	0.0067(0.0005)	3.873(0.010)	
distorted BiOCl	Bi-O	4.0(0.4)	0.0087(0.0007)	2.295(0.008)	0.004
	Bi-Cl	3.6(0.7)	0.0210(0.0015)	3.055(0.008)	
	Bi-Bi1	3.6(0.4)	0.0061(0.0005)	3.716(0.010)	
	Bi-Bi2	3.8(0.4)	0.0061(0.0005)	3.870(0.012)	

Table S3. Performance comparison of standard BiOCl and distorted BiOCl nanoplates with the state-of-the-art Bi/Sn-based electrocatalysts in the recent years.

Ref.	Electrocatalyst	Electrolyte	Potential (V vs. RHE)	FE _{HCOOH} (%)	$j_{\text{HCOOH,max}}$ (mA cm ⁻²)
This work	standard BiOCl	0.5 M KHCO ₃	-0.9	58	-12
	distorted BiOCl			92	-29
[7]	Cu foam@BiNW	0.5 M NaHCO ₃	-0.9	93	-35
[10]	SnO ₂	0.1 M KHCO ₃	-1.1	65	-8
[29]	Bi derived from BiOCl	0.1 M KHCO ₃	-0.8	92	-3.8
[30]	Bi NS	0.5 M NaHCO ₃	-0.9	96	-16
[32]	Bi NT	0.5 M KHCO ₃	-1.1	93	-55
[34]	Bi ₂ O ₃ NSs@MCCM	0.1 M KHCO ₃	-1.4	94	-18
[35]	Bi ₂ O ₂ CO ₃	0.5 M NaHCO ₃	-0.7	85	-11
[36]	Bi mesoporous nanosheet	0.5 M NaHCO ₃	-0.9	99	-15
[37]	BiOBr-templated catalysts	0.1 M KHCO ₃	-0.9	95	-58

Table S4. Free energy corrections for gas-phase species (eV).

Gaseous molecule and their free energy correction (eV)				
Species	E_{ZPE}	$\int Cv dT$	TS	G-Eelec(eV)
H ₂ (g)	0.284	0.091	0.403	-0.028
CO ₂	0.308	0.091	0.652	-0.253
CO	0.136	0.091	0.611	-0.384
H ₂ O	0.573	0.104	0.584	0.093
HCOOH	0.897	0.104	0.988	-0.013
Free energy corrections for surfaces and adsorbates on perfect BiOCl (eV)				
Species	E_{ZPE}	$\int Cv dT$	TS	G-Eelec(eV)
*COOH	0.575	0.105	0.232	0.448
*OCHO	0.594	0.111	0.237	0.468
HCOOH*	0.916	0.125	0.273	0.768
CO*	0.160	0.103	0.242	0.021
H*	0.290	0.011	0.015	0.286
Free energy corrections for surfaces and adsorbates on distorted BiOCl with single Cl defect (eV)				
Species	E_{ZPE}	$\int Cv dT$	TS	G-Eelec(eV)
*COOH	0.607	0.087	0.172	0.522
*OCHO	0.606	0.108	0.221	0.493
HCOOH*	0.911	0.116	0.247	0.78
CO*	0.160	0.101	0.232	0.029
H*	0.164	0.011	0.015	0.16
Free energy corrections for surfaces and adsorbates on distorted BiOCl with triple Cl defect (eV)				
Species	E_{ZPE}	$\int Cv dT$	TS	G-Eelec(eV)
*COOH	0.595	0.112	0.238	0.469
*OCHO	0.600	0.113	0.245	0.468
HCOOH*	0.920	0.117	0.244	0.793
CO*	0.163	0.094	0.215	0.042
H*	0.141	0.021	0.038	0.124
Free energy corrections for surfaces and adsorbates on BiOCl ultrathin nanosheets (eV)				
Species	E_{ZPE}	$\int Cv dT$	TS	G-Eelec(eV)
*COOH	0.613	0.107	0.216	0.504
*OCHO	0.603	0.110	0.230	0.483
HCOOH*	0.913	0.114	0.242	0.785
CO*	0.157	0.081	0.187	0.051
H*	0.157	0.010	0.013	0.153
Free energy corrections for surfaces and adsorbates on standard BiOCl-V_O nanosheets (eV)				
Species	E_{ZPE}	$\int Cv dT$	TS	G-Eelec(eV)

*COOH	0.604	0.110	0.228	0.485
*OCHO	0.602	0.111	0.236	0.477
HCOOH*	0.907	0.124	0.237	0.759
CO*	0.159	0.103	0.242	0.020
H*	0.138	0.014	0.020	0.132

References

1. J. P. Perdew, Burke, K., and Ernzerhof, M., *Phys. Rev. Lett.*, 1996, **77**, 3865.
2. H. J. Monkhorst and J. D. Pack, *Phys. Rev. B*, 1976, **13**, 5188–5192.
3. D. Vanderbilt, *Phys. Rev. B Condens. Matter.*, 1990, **41**, 7892–7895.
4. A. Tkatchenko and M. Scheffler, *Phys. Rev. Lett.*, 2009, **102**, 073005.
5. G. Kresse and J. Hafner, *Phys. Rev. B Condens. Matter.*, 1994, **49**, 14251–14269.
6. S. Ehrlich, J. Moellmann, W. Reckien, T. Bredow and S. Grimme, *Chemphyschem*, 2011, **12**, 3414–3420.
7. J. K. Nørskov, Rossmeisl, J., Logadottir, A., and Lindqvist, L., *J. Phys. Chem. B*, 2004, **108**, 17886–17892.
8. A. A. Peterson, F. Abild-Pedersen, F. Studt, J. Rossmeisl and J. K. Nørskov, *Energy Environ. Sci.*, 2010, **3**, 1311–1315.
9. D. Rao, L. Zhang, Y. Wang, Z. Meng, X. Qian, J. Liu, X. Shen, G. Qiao and R. Lu, *J. Phys. Chem. C*, 2017, **121**, 11047–11054.
10. X. Zheng, P. De Luna, F. P. García de Arquer, B. Zhang, N. Becknell, M. B. Ross, Y. Li, M. N. Banis, Y. Li, M. Liu, O. Voznyy, C. T. Dinh, T. Zhuang, P. Stadler, Y. Cui, X. Du, P. Yang and E. H. Sargent, *Joule*, 2017, **1**, 79427805.
11. H. Mistry, Y. W. Choi, A. Bagger, F. Scholten, C. S. Bonifacio, I. Sinev, N. J. Divins, I. Zegkinoglou, H. S. Jeon, K. Kisslinger, E. A. Stach, J. C. Yang, J. Rossmeisl and B. Roldan Cuenya, *Angew. Chem. Int. Ed.*, 2017, **56**, 11394–11398.
12. S. P. Liu, M. Zhao, W. Gao and Q. Jiang, *ChemSusChem*, 2017, **10**, 387–393.
13. V. Tripković, E. Skúlason, S. Siahrostami, J. K. Nørskov and J. Rossmeisl, *Electrochim. Acta*, 2010, **55**, 7975–7981.